Intersubband plasmon excitations in doped carbon nanotubes

Daria Satco,[1,2,*] Ahmad R. T. Nugraha,[2,†] M. Shoufie Ukhtary,[2] Daria Kopylova,[1]
Albert G. Nasibulin,[1,3] and Riichiro Saito[2]

[1]*Skolkovo Institute of Science and Technology, Moscow 143026, Russia*
[2]*Department of Physics, Tohoku University, Sendai 980-8578, Japan*
[3]*Department of Applied Physics, Aalto University, Aalto 00076, Finland*

(Received 28 November 2018; published 4 February 2019)

We theoretically investigate intersubband plasmon excitations in doped single-wall carbon nanotubes (SWNTs) by examining the dependence of plasmon frequency on the nanotube diameter, chirality, and Fermi energy. The intersubband plasmons can be excited by light with polarization perpendicular to the nanotube axis and thus the plasmon excitations correspond to optical transitions between the two different subbands, which are sensitive to the Fermi energy. In every SWNT, this mechanism leads to the emergence of the optical absorption peak at the plasmon frequency for a given Fermi energy, E_F. The plasmon frequencies calculated for many SWNTs with diameter $d_t < 2$ nm exhibit a dependence on $(1/d_t)^{0.7}$ and the frequencies are further affected by Fermi energy as $E_F^{0.25}$. With this knowledge, it is possible to develop a map of intersubband plasmon excitations in doped SWNTs that could be useful to quickly estimate the doping level and also be an alternative way to characterize nanotube chirality.

DOI: 10.1103/PhysRevB.99.075403

I. INTRODUCTION

For many years, single wall carbon nanotubes (SWNTs) have been an important platform to study optical properties of one-dimensional (1D) materials, especially due to their geometry-dependent optical absorption [1–4] and also due to their potential applications for optoelectronic devices [5–8]. Of the wide interest in the optical properties of SWNTs, a particular problem of the doping effects on the absorption of linearly polarized light is worth investigating. So far, previous studies have confirmed that *undoped* SWNTs absorb only light with polarization parallel to the nanotube axis [9–13], so that when the light polarization is perpendicular to the nanotube axis the undoped SWNTs do not show any absorption peak due to the depolarization effect [11,14]. The optical absorption in the case of parallel polarization can be understood in terms of the E_{ii} *interband* excitations from the ith valence to the ith conduction energy subbands, either in single-particle [2,9,11] or excitonic pictures [15–18]. On the other hand, much uncertainty still exists about what happens in the case of *doped* SWNTs for the linearly polarized light.

Recently, Sasaki *et al.* suggested that doped (undoped) SWNT absorb light with polarization perpendicular (parallel) to the nanotube axis [19,20]. Furthermore, Yanagi *et al.* [21] experimentally gave evidence that the doped SWNTs absorb light with the perpendicular polarization within the near-infrared range of a photon energy (∼0.8−1.2 eV). This energy range is similar to that when undoped SWNTs absorb light with the parallel polarization. Senga *et al.* showed consistent absorption peaks for isolated metallic SWNTs that are unintendedly doped on the TEM supporting grid during electron energy-loss spectroscopy (EELS) measurements [22,23]. Yanagi *et al.* proposed that the absorption peaks are related with *intersubband* plasmon excitations [21], i.e., the optical transitions with energies E_{ij} occur collectively between two electronic subbands i and j as a response to the perpendicularly polarized light. Unlike the *interband* excitations E_{ii} which take place from the valence to the conduction bands, the *intersubband* plasmon excitations E_{ij} occur within the conduction band or within the valence band.

It should be noted that in the EELS experiment by Senga *et al.* we can also see another plasmonic peak around 6 eV, the so-called π plasmon, which is *not* excited by light with perpendicular polarization but with parallel polarization [22,23]. Observations of the π-plasmons in SWNTs [24,25] or any graphitic materials [26–28], either doped or undoped, are quite common in the earlier EELS experiments and the peaks are assigned unambiguously. Lin and Shung two decades ago theoretically explained the origin of π plasmons in the SWNTs as a result of collective interband excitations of the π-band electrons [29,30]. On the other hand, the theory for plasmons excited in doped SWNTs with perpendicularly polarized light is just available recently by Sasaki *et al.* [19,20] and Garcia de Abajo [31], in which they discussed how the plasmon frequency (ω_p) in a doped SWNT depends on its diameter (d_t) and Fermi energy (E_F). However, the dependence of ω_p on d_t and E_F was analyzed within the Drude model, which is not relevant to *intersubband* transitions but it deals with *intrasubband* transitions. In this sense, there is a necessity to properly describe the intersubband plasmons in the doped SWNTs for any SWNT structure or chirality.

*daria.satco@skoltech.ru
†nugraha@flex.phys.tohoku.ac.jp

In this paper, we show our calculation of plasmon frequencies for the doped SWNTs as a function of diameter and the Fermi energy, considering all SWNTs with different chiralities in the range of $0.5 < d_t < 2$ nm. The calculated plasmon frequencies exhibit a diameter dependence of $(1/d_t)^{0.7}$ and are further dependent on the Fermi energy as $E_F^{0.25}$. This scaling of plasmon frequency differs with that predicted by the Drude model, $\omega_p \propto (E_F/d_t)^{0.5}$ [19,31], hence indicating the difference of the *intersubband* transitions (current work) from the *intrasubband* transitions (the Drude model). We further consider optical absorption at the plasmon frequencies caused by intersubband transitions within the conduction and valence bands, corresponding to $E_F > 0$ and $E_F < 0$, respectively. We find that the most dominant plasmonic transition, which we label as P_{ij} at a certain energy E_{ij} (following the notation introduced by Bondarev [32] for the *interband* plasmon at E_{ii}), changes with Fermi energy from a P_{ij} to another $P_{i'j'}$. For the smaller (larger) nanotube diameter, we need higher (lower) E_F to excite the plasmon. Using the fitting formula for the plasmon frequency provided in this paper, one can estimate the Fermi energy in the doped SWNTs by means of optical spectroscopy, as well as EELS. Furthermore, experimentalists can also search for intersubband plasmons in isolated SWNTs with various chiralities, not only limited to SWNTs bundles.

The rest of this paper is organized as follows. In Sec. II, we describe how to calculate the plasmon frequency for a given SWNT starting from the dielectric function of the SWNT. The complex dielectric function in this paper is calculated within the self-consistent-field approach by considering dipole approximation for optical matrix elements from which there exist selection rules for different light polarizations. In Sec. III, we discuss the main results of intersubband plasmon frequencies, including the opportunity to map them into a unified picture of $\omega_p \propto (E_F^{0.25}/d_t^{0.7})$. We justify the fitting by means of graphene plasmon dispersion, considering the model of the rolled graphene sheet for a SWNT. Finally, we give conclusions and future perspectives in Sec. IV.

II. THEORETICAL METHODS

A. Defining plasmons from dielectric function

We consider a SWNT subjected to perturbation by light whose vector potential, electric field, and magnetic field are denoted by **A**, **E**, and **B**, respectively. The vector potential of the electric field of incident light at the position of **r** and time t is given by

$$\mathbf{A}(\mathbf{r}, t) = A_0 \mathbf{n} \cos(\mathbf{q} \cdot \mathbf{r} - \omega t), \tag{1}$$

where A_0, ω, **q**, and **n** denote the vector potential amplitude, angular frequency, wave vector in the direction of propagation, and unit vector of polarization direction, respectively. The magnetic and electric fields are related with **A** by $\mathbf{E}(\mathbf{r}, t) = -d\mathbf{A}/dt$ and $\mathbf{B}(\mathbf{r}, t) = \nabla \times \mathbf{A}$, respectively. These quantities are important in the calculation of optical matrix elements, as derived in details in Appendix A.

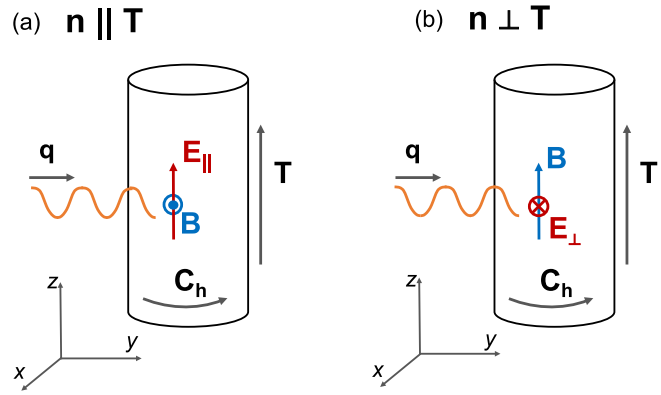

FIG. 1. Two geometries of propagating linearly polarized light with electrical field being polarized in (a) parallel and (b) perpendicular directions with respect to the nanotube axis.

We will discuss two cases of **n**: parallel and perpendicular to the nanotube axis, shown in Fig. 1. We refer to the two cases as the parallel polarization and perpendicular polarization. The nanotube axis is denoted by the translational vector **T** in three dimension as shown in Fig. 1(a) for $\mathbf{n} \parallel \mathbf{T}$ and Fig. 1(b) for $\mathbf{n} \perp \mathbf{T}$. If we imagine the SWNT as a rolled-up graphene sheet, the nanotube axis in the unrolled sheet is always perpendicular to the chiral vector $\mathbf{C}_h$, thus the unit cell of the SWNT is defined by the rectangular whose boundaries are $\mathbf{C}_h$ and **T** [33]. The chiral vector $\mathbf{C}_h$ in the basis of two-dimensional (2D) lattice vectors of graphene uniquely identifies the SWNT structure by $\mathbf{C}_h = (n, m)$, where the set of integers (n, m) is known as the chirality.

In both optical spectroscopy and EELS, plasmons are observed as prominent peaks in the spectra. The intensity of optical absorption is proportional to $\mathrm{Re}(\sigma/\varepsilon)$ [34], where σ and ε are, respectively, optical conductivity and dielectric function as a function of light frequency ω. Note that the dielectric function in the optical absorption accounts for the depolarization effect, which means that the screening of the external electrical field is included in the calculation of optical absorption for both perpendicular and parallel polarizations of light. Indeed, the depolarization effect is essential for explaining the anisotropy of optical absorption in SWNTs [14,35,36]. On the other hand, the intensity of EELS is proportional to the energy loss-function, $\mathrm{Im}(-1/\varepsilon)$ [37,38], that describes the excitation spectrum of solid by inelastic scattering of electrons at small angles. The plasmon peaks originate from zero points of the real part of $\varepsilon(\omega)$, i.e., $\mathrm{Re}[\varepsilon(\omega)] = 0$, followed by a relatively small value of its imaginary part, $\mathrm{Im}[\varepsilon(\omega)]$, in comparison with the maximum of $\mathrm{Im}[\varepsilon(\omega)]$.

According to the Maxwell equations, the optical conductivity σ is related to the dielectric function ε as follows:

$$\varepsilon(\omega) = 1 + i\frac{4\pi\sigma(\omega)}{\omega L \varepsilon_s}, \tag{2}$$

where ε_s is surrounding dielectric permittivity ($\varepsilon_s = 2$ for SWNT film [39]) and L is the effective thickness of the material ($L = d_t$ for SWNT). We calculate $\varepsilon(\omega)$ within the

self-consistent-field approach in the following form [29,40]:

$$\varepsilon(\omega) = \varepsilon_0 + \left[\frac{8\pi e^2}{\hbar\omega A_t} \left(\frac{\hbar^2}{m} \right)^2 \sum_{\substack{s_1,\, s_2 \\ \mu_1,\, \mu_2}} \int_{BZ} \frac{dk}{2\pi} \left| \mathcal{M}_{s_1 s_2}^{\mu_1 \mu_2}(k) \right|^2 \frac{f\left[E_{s_1,\mu_1}(k)\right] - f\left[E_{s_2,\mu_2}(k)\right]}{E_{s_2,\mu_2}(k) - E_{s_1,\mu_1}(k) - \hbar\omega + i\Gamma} \frac{1}{E_{s_2,\mu_2}(k) - E_{s_1,\mu_1}(k)} \right], \tag{3}$$

where $\mathcal{M}_{s_1 s_2}^{\mu_1 \mu_2}(k) = \langle s_2, \mu_2, k | \mathbf{n} \cdot \boldsymbol{\nabla} | s_1, \mu_1, k \rangle$ is the optical matrix element corresponding to a transition from an initial state (s_1, μ_1) to a final state (s_2, μ_2) [41], $A_t = \pi (d_t/2)^2$ is the cross-section area of a SWNT, and $f[E(k)]$ is Fermi-Dirac distribution function. The electron wave function $|s, \mu, k\rangle$ is related with the subband energy $E_{s,\mu}(k)$, where $s = c$ ($s = v$) for a conduction (valence) subband and μ is the index for the cutting line, which represents the 1D Brillouin zone (BZ) of the SWNT [33] with the electron wave vector k. The cutting lines are plotted in the 2D BZ of graphene with index $\mu = 1, 2, \ldots, N$. The value of N depends on (n, m), according to the formula $N = [2(n^2 + m^2 + nm)]/d_R$, where $d_R = \gcd(2n + m, 2m + n)$.

In Eq. (3), Γ is the broadening factor that accounts for relaxation processes in optical transitions resulting in finite lifetime τ of the electron state. Here we simply assume that Γ does not depend on ω or E_F but is constant, $\Gamma = 50$ meV [42]. The numerical integration over k is implemented by the left Riemann sums approximation, where the step dk is chosen to reach an accuracy $\Delta\varepsilon/\varepsilon = \pm 0.01$, corresponding to $dk = \Gamma/(5\hbar v_F)$, where $v_F = 10^6$ m/s is the Fermi velocity in graphene.

To obtain the energy band structure of carbon nanotubes, we adopt the zone-folding approximation of graphene with long-range atomic interactions up to the third nearest-neighbor transfer integrals, or the so-called third-nearest-neighbor tight-binding (third NNTB) model [43,44]. Although this approach does not include the curvature effect, the resulting band structure is sufficiently accurate for SWNTs with diameter larger than 1 nm [45]. Note that in contrast to the simplest tight-binding approach, the subbands within the valence and conduction bands in the third NNTB model are not further symmetric with respect to $E = 0$. Therefore, the SWNTs properties are more sensitive to the doping type (n-type or p-type) as usually observed in experiments.

B. Optical selection rules

Both dielectric function and optical conductivity are obtained by taking summation of different contributions from all possible pairs of (s_1, μ_1) and (s_2, μ_2). Although the summation in Eq. (3) is performed over all the cutting lines in valence and conduction bands, only a limited number of subbands gives nonzero contribution. The $(s_1, \mu_1) \rightarrow (s_2, \mu_2)$ transition is contributive when $\mathcal{M}_{s_1,s_2}^{\mu_1,\mu_2}(k)$ is nonzero (optical selection rules) and the Pauli exclusion principle is satisfied [the difference of Fermi-Dirac distributions in Eq. (3) is nonzero]. The concept of optical selection rules for SWNTs was originally discussed by Ajiki and Ando [9], who formulated the optical matrix elements by current-density operator. They proved that the allowed transitions are always vertical ($k_1 = k_2$) and the cutting line index should be conserved for parallel polarization ($\mu_1 = \mu_2$). On the other hand, the optical transition for perpendicular polarization occurs within nearest-neighbor cutting lines, $\mu_2 = \mu_1 \pm 1$.

For the sake of completeness, we rederive the optical selection rules within the dipole approximation. For parallel polarization, the optical matrix elements are

$$\begin{aligned} \mathcal{M}_{s_1 s_2}^{\mu_1 \mu_2}(k_1, k_2) = & \sum_{\ell, \ell' = A,B} C_{k_2 \mu_2 \ell'}^{s_2 *} C_{k_1 \mu_1 \ell}^{s_1} \\ & \times \delta(k_1 - k_2) \delta(\mu_1 - \mu_2) \\ & \times \sum_j \mathbf{n}_{\parallel} \cdot \langle j, \ell' | \boldsymbol{\nabla} | 0, \ell \rangle e^{-i\mathbf{k}_2 \cdot \mathbf{R}(j)}, \end{aligned} \tag{4}$$

and for perpendicular polarization we obtain

$$\begin{aligned} \mathcal{M}_{s_1 s_2}^{\mu_1 \mu_2}(k_1, k_2) = & \sum_{\ell, \ell' = A,B} C_{k_2 \mu_2 \ell'}^{s_2 *} C_{k_1 \mu_1 \ell}^{s_1} \delta(k_1 - k_2) \\ & \times \frac{1}{2} (\delta(\mu_1 - \mu_2 - 1) + \delta(\mu_1 - \mu_2 + 1)) \\ & \times \sum_j \mathbf{n}_{\perp} \cdot \langle j, \ell' | \boldsymbol{\nabla} | 0, \ell \rangle e^{-i\mathbf{k}_2 \cdot \mathbf{R}(j)}. \end{aligned} \tag{5}$$

The detailed derivation for Eqs. (4) and (5), as well as the meaning of each variable in their right-hand sides, are given in Appendix A. It should be noted that the results of optical selection rules are the same either by considering dipole approximation or current-density operator [9].

When we discuss the plasma oscillations in the electron gas, all charges are considered equivalent and contributing to the collective motion. However, it is not the case for SWNTs, in which the electronic states consist of N subbands in both valence and conduction bands. The calculated plasmonic excitations in nanotubes show that the plasmon peak is dominated by a particular $(s_1, \mu_1) \rightarrow (s_2, \mu_2)$ transition. With this regard, and also for clarity in presenting our results, let us introduce a more convenient notation for the plasmonic transition that can be used generally for all (n, m) SWNTs. Here our target is to assign one-to-one correspondence between the $(s_1, \mu_1) \rightarrow (s_2, \mu_2)$ transition and the *intersubband* transition energy E_{ij}, similar to the notation adopted for the *interband* optical transitions E_{ii} [2,46]. The case of $s_1 \neq s_2$ is the *interband* transition, while the case of $s_1 = s_2$ (with $\mu_1 \neq \mu_2$) is the *intersubband* transition. The condition of $s_1 = s_2$ means that we consider the intersubband transition within the conduction (or valence) band. Therefore, instead of using the cutting line index μ, which strongly depends on the SWNT structure, we will label the cutting line by integers i starting from the cutting line closest to the K point. Two examples are shown in Figs. 2(b) and 2(c) for (10,5) semiconducting and (6,3) metallic SWNTs, respectively. It is

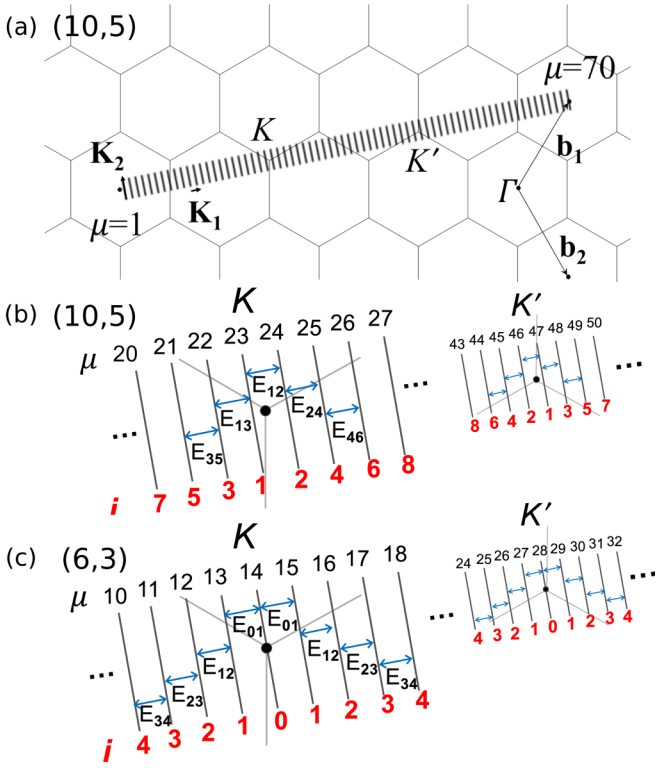

FIG. 2. (a) Cutting lines of the (10,5) SWNT on hexagonal 2D BZ, where $N = 70$. We also show a closer look at cutting lines around the K and K' points for (b) (10,5) semiconducting SWNT and (c) (6,3) metallic SWNT. In (b) and (c), two approaches are demonstrated to label the energy bands: with the cutting line index μ (upper) and with optical transition index i (lower). Intersubband transitions for perpendicular polarization are shown by arrows.

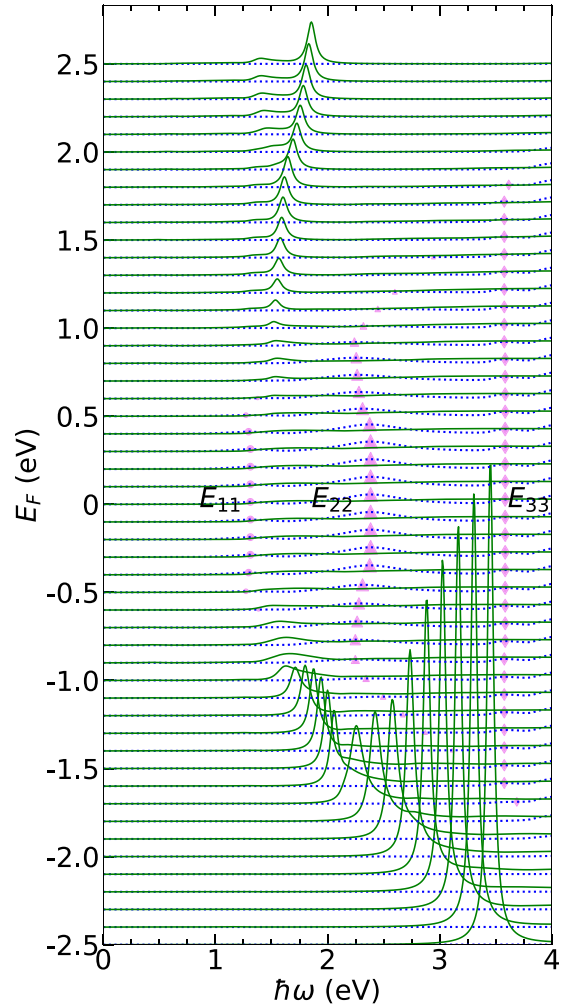

FIG. 3. Doping-induced evolution of optical absorption spectra in a (10,5) SWNT. Solid (dotted) lines represent perpendicular (parallel) polarization of light. Circles, triangles, and diamonds are a guide for eyes to trace the E_{11}, E_{22}, and E_{33} transition peaks in the case of parallel polarization. The absorption peaks in the case of parallel polarization are not due to intersubband plasmons, while the peaks in the case of perpendicular polarization are caused by intersubband plasmons, as discussed in the main text.

possible to analytically obtain the new cutting line indices (optical transition indices) around the K and K' points [47]. Then, the transitions can be enumerated according to the distance of the corresponding cutting line from the K or K' points [Fig. 2(b)], such as $E_{12}, E_{13}, E_{24}, E_{35}$, and E_{46} for a semiconducting SWNT. In the case of metallic SWNT [Fig. 2(c)], by excluding the trigonal warping effect [2], we can obtain transitions such as E_{01}, E_{12}, E_{23}, and so on, either going to the right or left direction away from the K (or K') point.

III. RESULTS AND DISCUSSION

A. Absorption spectra of doped SWNT

Let us first discuss the absorption spectra of doped SWNT for a particular (n, m). In Fig. 3, we plot $\mathrm{Re}(\sigma/\varepsilon)$ of the (10,5) SWNT as a function of photon energy $\hbar\omega$ for parallel and perpendicular polarization. Many spectra are plotted for different Fermi energies E_F from -2.5 to 2.5 eV. For $|E_F| < 0.5$ eV, since the first energy subband of conduction (valence) band is not occupied, we can observe interband transitions of all E_{ii}'s with $i \in \{1, 2, 3\}$ for the transitions between the valence and conduction bands. When we increase $|E_F|$ more than 0.5 eV, the E_{ii} peaks start to disappear from E_{11} to E_{33} because the ith subband in the conduction (valence) band begins to be occupied (unoccupied) for $i = 1, 2$, and so on. The position of E_{ii} peaks (circles, triangles, and diamonds for E_{11}, E_{22}, and E_{33}, respectively) is redshifted by increasing doping and then blueshifted before disappearing. The redshift of E_{ii} occurs because of the depolarization correction, which decreases with doping, whereas the blueshift attests the parabolic shape of the subbands. The depolarization correction can be seen as the inclusion of Coulomb interaction between electrons in the calculation of optical absorption [$\mathrm{Re}(\sigma/\varepsilon)$], since $\varepsilon(\omega) = 1 + iv_q\sigma(\omega)q^2/(e^2\omega)$, where $v_q = 2\pi e^2/q$ is the Coulomb potential and $q = 2/d_t$. Hence the dielectric function can be expressed as in Eq. (2). Without the inclusion of Coulomb interaction, the position of E_{ii} absorption peaks is constant by doping, not redshifted. Although we do not include the excitonic effect for simplicity, the presence of redshift in the E_{ii} peaks in our calculation is consistent with the previous work by Sasaki and Tokura [20]. It should be noted that, by the exclusion of excitonic effect, for $d_t = 2$ nm, the deviation

of the peak positions (defined as maxima of $\mathrm{Re}[\sigma(\omega)]$) is still less than 10% in comparison with the exciton Kataura plot [18].

While the ith subband is being occupied with electrons (or holes), the value of E_{ii} increases because the single-particle excitations occur only for the restricted k-regions, which are far from k_{ii} [2,11,47], where the interband energy distance is larger. When the subband is partially occupied, a new peak for perpendicular polarization appears. We expect that such a peak is related with intersubband plasmon excitations for several reasons: (1) $\mathrm{Re}(\varepsilon)$ has a zero point close to the peak position, (2) the peak position is different from the single-particle intersubband $i \to j$ transition, (3) the peak intensity strongly depends on Fermi energy and continuously increases even when the subbands are almost occupied and part of transitions is blocked, and (4) the blueshift with increasing the Fermi energy is opposite to the redshift for the single-particle excitation [39]. For highly positive doping $E_F > 1.9$ eV, the second smaller peak is observed around 1.4 eV as shown in Fig. 3. This peak is another type of plasmon, which differs from the first one at $1.5 - 1.8$ eV by the dominant contributions (see the more detailed discussion in Appendix B). Hereafter, we focus our attention to the first, main plasmon peak, since this one should easily be observed in experiments. The Fermi-energy dependent optical absorption shown in Fig. 3 is consistent with that previously discussed by Sasaki and Tokura [20] for the armchair (10,10) and zigzag (16,0) SWNTs. However, the present result shows additional plasmon peaks (Appendix B) and different doping-type dependence (for $E_F > 0$ and $E_F < 0$), which appears by introducing more accurate energy band calculation.

B. Plasmon excitation in SWNT

In Fig. 4(a), we plot the absorption peak position in the case of perpendicular polarization for the (10,5) SWNT as a function of E_F. The intensity of each peak is represented by the circle diameter. We attribute the peak as the plasmon peak and denote its frequency as ω_p when $\mathrm{Re}[\varepsilon(\omega_0)] = 0$ and ω_0 is close ($\leqslant$20 meV) to ω_p. Each point in Fig. 4(a) consists of several circles which correspond to different contributions from the transition of the cutting line pair $i \to j$ measured from the K point. We denote the dominant $i \to j$ contribution as P_{ij}, where the threshold for dominant contribution was chosen as 10% of maximum contribution for each peak. Here we omit the valence and conduction band indices (s_1, s_2) since the dominant transition is the intersubband transition, $s_1 = s_2$. One can clearly observe the kink shape of the function, as well as the existence of the second plasmon branch at lower frequencies for $E_F > 2$ eV (see Appendix B for details).

In Fig. 4(b), we display the density of states (DOS) and charge density as a function of Fermi energy for the (10,5) nanotube. The charge density for electrons at $E_F > 0$ is given by $\rho(E_F) = \int_0^\infty D(E) f(E) dE$, where $D(E)$ is the DOS. For holes at $E_F < 0$, we modify the charge-density formula by replacing the distribution function $f(E)$ with $1 - f(E)$. In Fig. 4(c), we show energy dispersion $E_{s,\mu}(k)$, where the energy subbands are labeled according to the approach discussed in Sec. II B. The kink positions for the plasmon energy and the

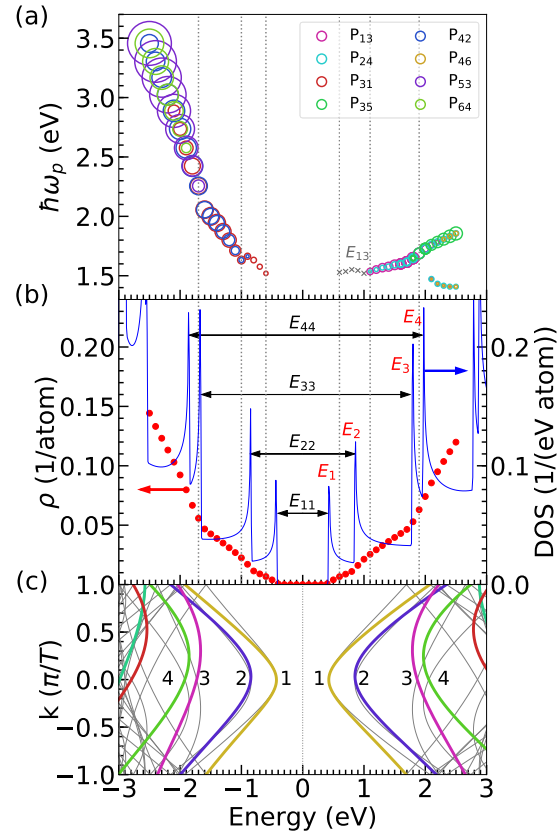

FIG. 4. (a) Plasmon frequency as a function of Fermi energy for the (10,5) SWNT. The radius of the circles corresponds to the intensity of the P_{ij} peak. Note that the weak peaks for $0.6 < E_F < 1.1$ eV are not plasmonic, but related to E_{13} absorption. (b) Density of states (solid line) and charge density (points) for (10,5) SWNT as a function of energy. Dotted vertical lines indicate the positions of kinks for plasmon frequency. (c) Energy band structure for the (10,5) SWNT. Colored bold lines correspond to the subbands coming from the cutting lines nearest to the K point. Thin solid lines correspond to the subbands from the other cutting lines in the presented energy range.

charge density $\rho(E_F)$ are shown to be consistent to each other [see grey dotted lines in Fig. 4(b)]. In the three-dimensional (3D) Drude model, the plasmon frequency is known to be proportional to the square root of charge density ($\omega_p^{\mathrm{3D}} \propto \sqrt{\rho}$). For carbon nanotubes, the Fermi energy dependence was predicted to be consistent with the 2D graphene result ($\omega_p^{\mathrm{2D}} \propto \sqrt{E_F}$) [31]. However, we see from Figs. 4(a) and 4(b) that the plasmon frequency is a function of $\rho(E_F)$, which in case of carbon nanotubes is the sum $\sum_{E_{ii}<E_F} \sqrt{E_F - E_{ii}}$.

The kink in $\rho(E_F)$ appears when E_F passes through the next van Hove singularity (E_i) as shown in Fig. 4(b), which is followed by the Pauli blockade of the ith subband and change in the dominant contribution to the plasmon from P_{ij} to another $\mathrm{P}_{i'j'}$, where $i' > i$ and $j' > j$ for $E_F > 0$ ($i' < i$ and $j' < j$ for $E_F < 0$). As seen from Fig. 4(a), the first dominant contribution is P_{13} (P_{31}), the second dominant contribution after the first kink is P_{24} (P_{42}), the third contribution after the second kink is P_{35} (P_{53}) for $E_F > 0$ ($E_F < 0$). The plasmon

intensity [radius of circle in Fig. 4(a)] increases with increasing the Fermi energy and inceasing $\rho(E_F)$.

The asymmetry of plasmon peak intensity with respect to the n-type and p-type doping is consistent with asymmetric nature of $\rho(E_F)$ for $E_F > 0$ and $E_F < 0$. The minimum plasmon frequency as well as the Fermi energy at which the plasmon is excited basically depend on the energy band structure. For example, in Fig. 4(a), the asymmetry in the values of E_{13} within valence and conduction bands influences the starting plasmon frequency ($\hbar\omega_p = 1.52$ eV for the valence band and $\hbar\omega_p = 1.54$ eV for the conduction band). Meanwhile, the number of subbands under or above the Fermi level within the valence or conduction band is essential for accumulating negative contribution to dielectric function to observe $\mathrm{Re}(\varepsilon) = 0$. Therefore, the interplay between the intersubband transitions determines the asymmetric nature of the plasmon peak intensity in the n-type and p-type doping. Note that at $E_F = 0$ eV, both real and imaginary parts of $\varepsilon(\omega)$ are positive in the energy range of 0–4 eV. In the case of p-doped (10,5) SWNT, the plasmon starts to appear at $E_F = 0.6$ eV, after the first subband becomes partially unoccupied, in which the condition of $\mathrm{Re}(\varepsilon) = 0$ is already satisfied. In the case of n-doping, the first small peak appears at $E_F = 1.1$ eV. However, since $\mathrm{Re}(\varepsilon) \neq 0$, this peak is still not a plasmon, but is a single-particle intersubband transition $1 \rightarrow 3$. It is observed when the first subband is partially occupied and when the depolarization effect, which was completely suppressing absorption before, is relaxed. The true plasmon peak appears at $E_F = 1.1$ eV, which corresponds to the second subband partially occupied. Thus, the condition to observe the plasmon in SWNT for perpendicularly polarized light is to shift the Fermi level up higher than the bottom of the second subband in the conduction band [19,21], or down lower than the top of the first subband in the valence band.

In Fig. 5(a), we plot intersubband and interband absorption spectra in case of perpendicular polarization for (10,5) SWNT and $E_F = 1.5$ eV. We define the absorption associated with the $i \rightarrow j$ transition as $A_{ij} = \mathrm{Re}(\sigma_\perp^{ij}/\varepsilon_\perp)$, where $\sigma_\perp^{ij}$ is

$$\sigma_\perp^{ij} = \frac{16}{d_t}\frac{e^2}{h}\left(\frac{\hbar^2}{m}\right)^2 \int_{-\pi/T}^{\pi/T} \frac{dk}{2\pi} |\mathcal{M}_{ij}^{\perp}(k)|^2 \times \frac{f(E_i(k)) - f(E_j(k))}{E_j(k) - E_i(k) - \hbar\omega + i\Gamma} \frac{1}{E_j(k) - E_i(k)}. \quad (6)$$

For $E_F > 0$, when we consider the interband transitions, the ith and the jth subbands come from the valence and conduction band, respectively. On the other hand, for the intersubband transitions, both subbands lie within the conduction band. The total absorption A_{tot} in Fig. 5(a) is contributed from all the interband and intersubband transitions. We see that the peak position and line shape of the absorption spectrum are consistent with those of EELS spectrum, which is given by $\mathrm{Im}(-1/\varepsilon)$.

As we already mentioned above, both optical conductivity and dielectric function are superpositions of contributions (σ_{ij}, ε_{ij}) from different transitions between the $i \rightarrow j$ subbands. To calculate absorption from the $i \rightarrow j$ transition A_{ij}, we take only the corresponding term from the conductivity σ_{ij}, while the dielectric function ($\varepsilon_\perp$) is calculated for all pairs

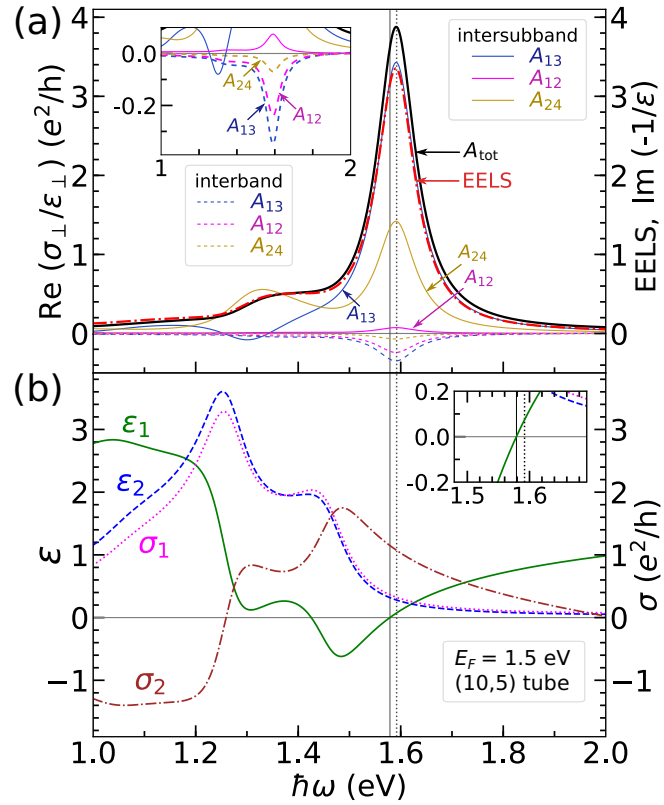

FIG. 5. (a) Absorption spectra for a doped (10,5) SWNT with $E_F = 1.5$ eV. Black bold solid line represents the total absorption A_{tot}, considering both the intersubband and interband transitions. Colored solid lines correspond to the dominant A_{13}, A_{24}, and A_{12} *intersubband* contributions. The EELS spectrum, $\mathrm{Im}(-1/\varepsilon)$, is plotted with red dash-dotted line. Colored dashed lines lines correspond to the interband absorptions with the same transition indices as the intersubband counterparts. Inset depicts the enlarged region for the interband peaks, which are about one order of magnitude smaller than the intersubband peaks. (b) Real (ε_1) and imaginary (ε_2) parts of dielectric function along with conductivity (σ_1 and σ_2) for (10,5) doped SWNT with $E_F = 1.5$ eV. Solid (dotted) vertical line corresponds to $\mathrm{Re}(\varepsilon) = 0$ [$\max(\mathrm{A_{tot}})$].

of interband and intersubband transitions according to Eq. (3). As an example, in the case of $E_F = 1.5$ eV in Fig. 4(a) two main contributions are $\mathrm{P_{13}}$ and $\mathrm{P_{24}}$. In Fig. 5(a), we see the peak value of A_{ij} for intersubband absorption (solid lines) is one order of magnitude larger than that for interband absorption (dashed lines), which clearly shows that the plasmon has an intersubband nature. One may notice that the same $\mathrm{P_{13}}$ and $\mathrm{P_{24}}$ transitions are dominant for both intersubband and interband absorptions. However, the contributions have different signs and different order of magnitude.

Although the interband transitions seem to give negligible contribution to the plasmon intensity, they affect the redshift of the zero point for the dielectric function [20], as shown in Fig. 5(b). In fact, the position of the maximum in absorption spectra (dotted vertical line) and the zero of $\mathrm{Re}[\varepsilon(\omega)]$ (solid vertical line) are slightly different (by $\sim$1 meV). This difference comes from $\mathrm{Im}[\varepsilon(\omega)]$, which decreases in the proximity of $\mathrm{Re}[\varepsilon(\omega)] = 0$, as well as $\mathrm{Im}[\sigma(\omega)]$ [Fig. 5(b)]. If the

dielectric function is a real function of ω, the zero value would give the exact position of plasmon, which is not the case for a complex $\varepsilon(\omega)$. Indeed, for $\varepsilon = \varepsilon_1 + i\varepsilon_2$ and $\sigma = \sigma_1 + i\sigma_2$, the absorption and the energy loss-function have the following form:

$$\mathrm{Im}\left(-\frac{1}{\varepsilon}\right) = \frac{1}{\varepsilon_2[1 + (\varepsilon_1/\varepsilon_2)^2]}, \tag{7}$$

$$\mathrm{Re}\left(\frac{\sigma}{\varepsilon}\right) = \frac{\sigma_2 + \sigma_1\left(\frac{\varepsilon_1}{\varepsilon_2}\right)}{\varepsilon_2[1 + (\varepsilon_1/\varepsilon_2)^2]}. \tag{8}$$

The maxima of $\mathrm{Im}(-1/\varepsilon)$ and $\mathrm{Re}(\sigma/\varepsilon)$ appear close to the $\varepsilon_1 = 0$, but not exactly at this point. The shift of the maxima strongly depends on slope of $\varepsilon_2(\omega)$ near the zero point of ε_1.

C. Mapping of intersubband plasmons

In Fig. 6, we plot energy of intersubband plasmon $\hbar\omega_p$ as a function of nanotube diameter d_t, where $0.5 < d_t < 2$ nm, for five Fermi energies from $E_F = 1$ to 2 eV. For $E_F = 1$ eV, plasmons are observed only in tubes with $d_t > 1$ nm. With increasing E_F, the number of tubes which have plasmonic excitations increases, since $E_{ii} < E_F$ ($E_{ii} \propto 1/d_t$) is satisfied for a large E_F even for smaller d_t nanotubes. Plasmon energies $\hbar\omega_p$, as well as their spreading for fixed d_t and E_F, are increasing with decreasing diameter. This indicates the presence of chirality dependence, which was neglected in the previous works [19,20,31]. We see that the dominant contributions for smaller diameters and higher Fermi energies come from the cutting line pairs, which are close to the K point. Therefore, the family spread due to the curvature effect is inherited by plasmon frequency. Hereafter, we focus on the Fermi energy and diameter dependence of plasmon frequency, since this information is useful for most experimental studies like the Kataura plot for optical absorption [49,50] or Raman spectroscopy [51]. Chirality dependence of plasmon energy is a challenging point for the present method, since the band structure calculation by adopting the third NNTB model is not satisfactory to build reliable chiral angle dependence or curvature effect [52].

We numerically fit the diameter and the Fermi energy dependence with power law, as shown in Fig. 7. The result is

$$\hbar\omega_p = (1.49 \pm 0.004)\frac{E_F^{0.25\pm0.003}}{d_t^{0.69\pm0.005}}\ \mathrm{eV}. \tag{9}$$

The d_t (in nm) and E_F (in eV) dependence in Fig. 7 can be understood from the dispersion of plasmon in graphene, which is shown in Fig. 8 [53]. The intersubband plasmons in doped SWNTs, which are nothing but the azimuthal plasmons [19], can be considered as the plasmons in the rolled graphene sheet, where we have the oscillations of charge around the nanotube axis. Rolling of graphene into SWNT results in the quantization of plasmon wave vector ($\mathbf{q_p}$) following the reciprocal lattice vector $\mathbf{K}_1$ [33] in the SWNT since we consider the transitions of electron between different cutting lines. The magnitude of the reciprocal lattice vector is inversely proportional to the diameter, i.e., $|\mathbf{K}_1| = 2/d_t$, similar to the wave vector of the electron along the circumferential direction ($q \propto d_t^{-1}$). From Fig. 8, we can see that the $\sqrt{q_p}$ dependence does not always hold for plasmon in graphene. The plasmon dispersion becomes almost linear to q_p as it enters the interband single-particle excitation ($\mathrm{SPE_{inter}}$) regime [53]. At the colored frequency range ($1.75\,E_F < \hbar\omega_p < 2.25\,E_F$) in Fig. 8, we fit the dispersion, where we get $\omega_p \propto q_p^{0.6986}$. Therefore, we expect $\omega_p \propto d_t^{-0.7}$ for the plasmon frequency of SWNT, which confirms our finding in Eq. (9). It is noted

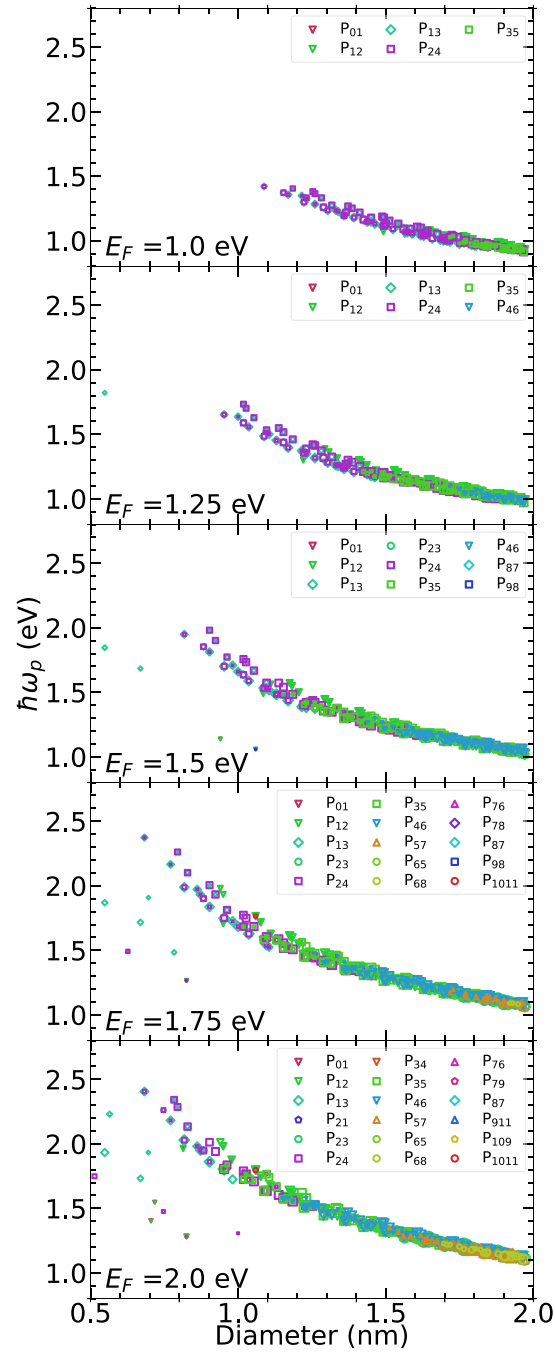

FIG. 6. Intersubband plasmon frequencies (major peak) for SWNTs of all different chiralities (n, m) with diameters from 0.5 to 2 nm. Five different Fermi energies from 1.0 to 2.0 eV are considered. The dominant contributions are pointed out for each plasmon (and thus each chirality) by specific marker types and colors. The size of the marker corresponds to the plasmon peak intensity [48].

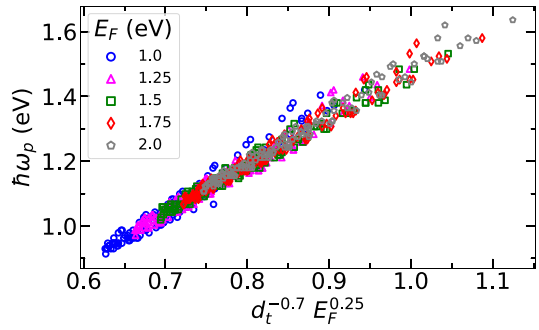

FIG. 7. Fitting of the intersubband plasmon energy as a function of nanotube diameter d_t and Fermi energy E_F. We consider SWNTs with $1 < d_t < 2$ nm and only the major plasmon peak.

that the $\omega_p \propto q_p^{0.7}$ of graphene's plasmon is at relatively higher frequency range compared with the obtained plasmon frequency range for SWNTs as shown in Fig. 6. This is owing to the fact that in SWNT, the lower limit of photon energy for single-particle excitation (the dash-dotted line in Fig. 8) would be smaller compared with the case of graphene due to the possible intersubband excitation of electron within the conduction band of SWNT. This lowering of energy limit for starting single-particle excitation by intersubband transition ($\text{SPE}_{\text{inter}}$) shifts the "almost" linear dispersion of plasmon in graphene to lower frequency range, too. Thus the fitting to "the almost linear dispersion" is justified.

The Fermi energy dependence of azimuthal plasmon in SWNT given by Eq. (9) can be also understood from the dispersion of plasmon in graphene shown in Fig. 8. Since the dispersion of plasmon in graphene is normalized to the Fermi energy as shown in Fig. 8, we can obtain the following

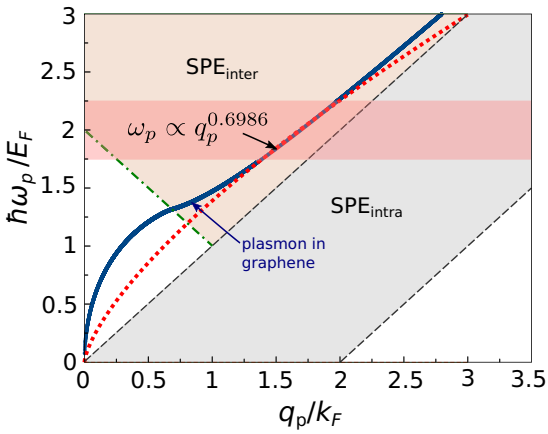

FIG. 8. Fitting of the plasmon dispersion of graphene. We found $\omega_p \propto q^{0.6986}$ within the horizontally dashed frequency range ($1.75\,E_F < \hbar\omega < 2.25\,E_F$) that could be related with the intersubband plasmon excitations in SWNTs. The other colored dashed areas correspond to the regime where the interband and intraband single-particle excitations occur in graphene, denoted by $\text{SPE}_{\text{inter}}$ and $\text{SPE}_{\text{intra}}$, respectively [53].

equation:

$$\hbar\omega_p = \left(\frac{q_p}{k_F}\right)^{\alpha} E_F = (q_p\hbar v_F)^{\alpha} E_F^{1-\alpha}, \tag{10}$$

where we use linear energy band of graphene, $E_F = \hbar v_F k_F$. Since $\omega_p \propto q_p^{0.6986}$, we expect the Fermi energy dependence to be $\omega_p \propto E_F^{0.3}$, which is not exact but close to the obtained power law in Eq. (9). The difference with the obtained power law comes from the fact that the electron energy bands of SWNTs are not exactly linear as in graphene. It is noted that if we have the $\sqrt{q_p}$ dependence of plasmon frequency in graphene, using Eq. (10), we will have $\omega_p \propto E_F^{0.5}$ as expected in the Drude model [19,31,53].

IV. CONCLUSION

We have systematically studied intersubband plasmon excitations in doped SWNTs as a function of diameter and the Fermi energy. The intersubband plasmons are excited due to the absorption of light with linear polarization perpendicular to the nanotube axis. The calculated plasmon frequency ω_p scales with the SWNT diameter d_t and the Fermi energy E_F as $\omega_p \propto (E_F^{0.25}/d_t^{0.7})$, which is a direct consequence of collective intersubband excitations of electrons in the doped SWNTs, but *not* a result of intraband transitions described by the Drude model. We also show that more than one branch of intersubband plasmons occurs even in one nanotube chirality. Our mapping of intersubband plasmon frequency may serve as a guide for experimentalists to search intersubband plasmons in many different SWNTs.

ACKNOWLEDGMENTS

D.S. thanks Skolkovo Institute of Science and Technology for financially supporting a three-month visit to Tohoku University for working on most parts of this project. A.R.T.N. acknowledges the Interdepartmental Program for Multidimensional Materials Science Leaders in Tohoku University. M.S.U. and R.S. acknowledge JSPS KAKENHI Grants No. JP18J10199 and No. JP18H01810, respectively. A.G.N. acknowledges Russian Science Foundation (Project No. 17-19-01787).

APPENDIX A: OPTICAL MATRIX ELEMENTS

The Schrödinger equation for a SWNT is given by

$$H(\mathbf{r})\psi_{\mathbf{k}}^s(\mathbf{r}) = E_{\mathbf{k}}^s\psi_{\mathbf{k}}^s(\mathbf{r}), \tag{A1}$$

where $H(\mathbf{r})$ is the real-space Hamiltonian, $\mathbf{k}$ is the electron wave vector, and $s = c$ ($s = v$) denotes the conduction (valence) band. The wave function $\psi_{\mathbf{k}}^s(r)$ can be expanded by a linear combination of the Bloch functions $\phi_{\mathbf{k}\ell}(r)$ as follows:

$$\psi_{\mathbf{k}}^s(\mathbf{r}) = \sum_{\ell=A,B} C_\ell^s(\mathbf{k})\phi_{\mathbf{k}\ell}(\mathbf{r}), \tag{A2}$$

where $C_\ell^s(\mathbf{k})$ is the coefficient for the state $\mathbf{k}$. The Bloch function is expressed by

$$\phi_{\mathbf{k}\ell}(\mathbf{r}) = \frac{1}{\sqrt{N}}\sum_j e^{i\mathbf{k}\cdot\mathbf{R}(j)}\chi(\mathbf{R}(j) - \mathbf{r}_\ell - \mathbf{r}), \tag{A3}$$

where $\chi(\mathbf{r})$ denotes the $2p_z$ atomic orbital, $\mathbf{R}(j) = j_1\mathbf{a}_1 + j_2\mathbf{a}_2$ gives the position of the jth unit cell (with $\mathbf{a}_1$ and $\mathbf{a}_2$ unit vectors of hexagonal unit cell [33]), $\mathbf{r}_\ell$ is the position of ℓth atom (A or B) in the jth unit cell, and N is the number of unit cells. Substituting Eq. (A2) into Eq. (A1) we obtain

$$\frac{1}{\sqrt{N}}\sum_{\ell=A,B} C_\ell^s(\mathbf{k})\sum_j e^{i\mathbf{k}\cdot\mathbf{R}(j)}H(\mathbf{r})\chi(\mathbf{R}(j)-\mathbf{r}_\ell-\mathbf{r})$$

$$= E_\mathbf{k}^s\frac{1}{\sqrt{N}}\sum_{\ell=A,B} C_\ell^s(\mathbf{k})\sum_j e^{i\mathbf{k}\cdot\mathbf{R}(j)}\chi(\mathbf{R}(j)-\mathbf{r}_\ell-\mathbf{r}). \quad \text{(A4)}$$

One can rewrite Eq. (A4) in a matrix form multiplying $\chi(\mathbf{R}(\mathbf{0})-\mathbf{r}_{\ell'}-\mathbf{r})$ to Eq. (A4), to obtain

$$\sum_{\ell=A,B} C_\ell^s(\mathbf{k})H_{\mathbf{k}\ell'\ell} = \sum_{\ell=A,B} E_\mathbf{k}^s C_\ell^s(\mathbf{k})S_{\mathbf{k}\ell'\ell}, \quad \text{(A5)}$$

where $H_{\mathbf{k}\ell'\ell}$ and $S_{\mathbf{k}\ell'\ell}$ are 2×2 Hamiltonian and overlap matrices, respectively, defined by

$$H_{\mathbf{k}\ell'\ell} = \sum_j e^{i\mathbf{k}\cdot(\mathbf{R}(j))}H_{\ell'\ell}(j), \quad \text{(A6)}$$

$$S_{\mathbf{k}\ell'\ell} = \sum_j e^{i\mathbf{k}\cdot(\mathbf{R}(j))}S_{\ell'\ell}(j), \quad \text{(A7)}$$

and

$$H_{\ell'\ell}(j) = \int d\mathbf{r}\chi(\mathbf{R}(\mathbf{0})-\mathbf{r}_{\ell'}-\mathbf{r})H\chi(\mathbf{R}(j)-\mathbf{r}_\ell-\mathbf{r}), \quad \text{(A8)}$$

$$S_{\ell'\ell}(j) = \int d\mathbf{r}\chi(\mathbf{R}(\mathbf{0})-\mathbf{r}_{\ell'}-\mathbf{r})\chi(\mathbf{R}^l(j)-\mathbf{r}_\ell-\mathbf{r}). \quad \text{(A9)}$$

$H_{\ell'\ell}(j)$, $S_{\ell'\ell}(j)$ are considered up to the third nearest-neighbor sites. Thus we come to the generalized problem for eigenvectors and eigenvalues of the form

$$H_\mathbf{k}\mathbf{C}_\mathbf{k}^s = E_\mathbf{k}^s S_\mathbf{k}\mathbf{C}_\mathbf{k}^s, \quad \text{(A10)}$$

where $E_\mathbf{k}^s = \{E_\mathbf{k}^v, E_\mathbf{k}^c\}$ gives the energy of valence and conduction subbands for particular SWNT and vector $\mathbf{C}_\mathbf{k}^s = (C_A^s(\mathbf{k}), C_B^s(\mathbf{k}))^T$ gives the coefficients for the wave function represented by Eq. (A2). Within the zone-folding approach, Eq. (A10) is solved for Hamiltonian of 2D graphene, while the wave vector is taken as quasi-1D BZ for SWNT given by [33]

$$\mathbf{k} = k\frac{\mathbf{K_2}}{|\mathbf{K_2}|} + \mu\mathbf{K_1}, \quad \left(\mu = 1,\ldots,N; -\frac{\pi}{T}\leqslant k\leqslant\frac{\pi}{T}\right), \quad \text{(A11)}$$

where T is the length of translational vector $\mathbf{T}$, $N = [2(n^2+m^2+nm)]/d_R$ is the number of cutting lines and $\mathbf{K}_2$ denotes 1D reciprocal lattice vector [33]. We adopt the wave-vector notation of Eq. (A11) to the single-electron wave function in carbon nanotube as bra-ket style as $|s,\mu,k\rangle \equiv \psi_\mathbf{k}^s(\mathbf{r})$.The single-particle Hamiltonian in the presence of external electromagnetic field is given by

$$H(\mathbf{r},t) = H(\mathbf{r}) + \frac{i\hbar e}{m}\mathbf{A}(\mathbf{r},t)\cdot\nabla, \quad \text{(A12)}$$

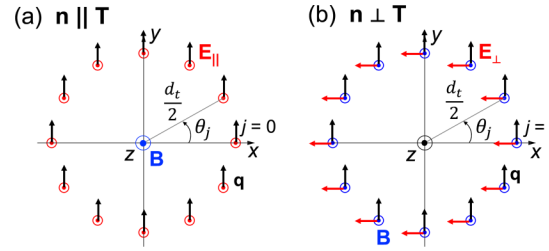

FIG. 9. Projections of probe photon wave vector $\mathbf{q}$ and electric field $\mathbf{E}$ onto nanotube cross section for (a) parallel polarization and (b) perpendicular polarization.

where $e>0$ is elemental charge and m is the mass of electron. The optical matrix element is given by $\langle s_2,\mu_2,k_2|\frac{i\hbar e}{m}\mathbf{A_q}\cdot\nabla|s_1,\mu_1,k_1\rangle$, where $\mathbf{A_q}$ is Fourier component of the vector potential $\mathbf{A}(\mathbf{r},t) = A_0\mathbf{n}\cos(\mathbf{q}\cdot\mathbf{r}-\omega t)$. For the light propagating parallel to the nanotube axis ($\mathbf{n}\parallel\mathbf{T}$) [Fig. 9(a)], $\mathbf{A_q}$ in the jth unit cell can be expressed as [54]

$$\mathbf{A_q}^{||}(\mathbf{R}(j)) = A_0\mathbf{n}_{||}e^{i\mathbf{q}\cdot\mathbf{R}(j)}$$

$$= A_0\mathbf{n}_{||}\left(1+iq\frac{d_t}{2}\sin\theta_j\right), \quad \text{(A13)}$$

In the case of perpendicularly polarized light ($\mathbf{n}\perp\mathbf{T}$) [Fig. 9(b)], $\mathbf{A_q}$ is expressed as

$$\mathbf{A_q}^{\perp}(\mathbf{R}(j)) = A_0\cos\theta_j\mathbf{n}_\perp e^{i\mathbf{q}\cdot\mathbf{R}(j)}$$

$$= \frac{A_0}{2}\mathbf{n}_\perp(e^{i\theta_j}+e^{-i\theta_j})\left(1+iq\frac{d_t}{2}\sin\theta_j\right), \quad \text{(A14)}$$

where we take the direction of $\mathbf{n}$ as $\mathbf{n}_{||} = (0,0,1)$ and $\mathbf{n}_\perp = (1,0,0)$. We also take into account the fact that qd_t is sufficiently small compared with the unity, which means that in both cases the dominant contribution to matrix element comes from the first term, whereas the second term including $q = |\mathbf{q}|$ can be neglected, which is known as the dipole approximation. Hereafter we will consider only the dominant terms. The optical matrix element in tight-binding approximation of Eq. (A2) has the following form:

$$\langle s_2,\mu_2,k_2|\mathbf{A_q}\cdot\nabla|s_1,\mu_1,k_1\rangle$$

$$= \frac{1}{N}\sum_{\ell,\ell'=A,B} C_{k_2\mu_2\ell'}^{s_2*}C_{k_1\mu_1\ell}^{s_1}\sum_{j,j'} e^{-i\mathbf{k}_2\cdot\mathbf{R}(j')}e^{i\mathbf{k}_1\mathbf{R}(j)}$$

$$\times\langle j',\ell'|\mathbf{A_q}(\mathbf{R}(j))\cdot\nabla|j,\ell\rangle, \quad \text{(A15)}$$

where $|j,\ell\rangle = \chi(\mathbf{R}(j)-\mathbf{r}_\ell-\mathbf{r})$ is the bra-ket form for the atomic orbital introduced in Eq. (A3). Let us discuss Eq. (A15) for the two cases of parallel and perpendicular polarization one by one.

1. Perpendicular polarization

When we put Eq. (A14) to Eq. (A15), we get

$$\begin{aligned}\langle s_2,\mu_2,k_2|\mathbf{A_q}\cdot\nabla|s_1,\mu_1,k_1\rangle &= \frac{A_0}{N}\sum_{\ell,\ell'=A,B} C^{s_2*}_{k_2\mu_2\ell'}C^{s_1}_{k_1\mu_1\ell}\sum_{j,j'}\mathbf{n}_\perp\cdot\langle j',\ell'|\nabla|j,\ell\rangle\frac{1}{2}(e^{i(\mathbf{k}_1\cdot\mathbf{R}(j)-\mathbf{k}_2\cdot\mathbf{R}(j')-\theta_j)}+e^{i(\mathbf{k}_1\cdot\mathbf{R}(j)-\mathbf{k}_2\cdot\mathbf{R}(j')+\theta_j)})\\ &= \frac{A_0}{N}\sum_{\ell,\ell'=A,B} C^{s_2*}_{k_2\mu_2\ell'}C^{s_1}_{k_1\mu_1\ell}\sum_{j}\frac{1}{2}(e^{i((\mathbf{k}_1-\mathbf{k}_2)\cdot\mathbf{R}(j)-\theta_j)}+e^{i((\mathbf{k}_1-\mathbf{k}_2)\cdot\mathbf{R}(j)+\theta_j)})\\ &\quad\times\sum_{j'}\mathbf{n}_\perp\cdot\langle j',\ell'|\nabla|j,\ell\rangle e^{-i\mathbf{k}_2\cdot(\mathbf{R}(j')-\mathbf{R}(j))}. \end{aligned}\tag{A16}$$

Here we define 2D unit vectors originated from carbon nanotube lattice vectors $\mathbf{C}_h$, $\mathbf{T}$ [54]:

$$\mathbf{e}_C=\frac{\mathbf{C}_h}{|\mathbf{C}_h|}=\frac{\mathbf{K}_1}{|\mathbf{K}_1|},\quad \mathbf{e}_T=\frac{\mathbf{T}}{|\mathbf{T}|}=\frac{\mathbf{K}_2}{|\mathbf{K}_2|}.\tag{A17}$$

Then vectors $\mathbf{k}_1$, $\mathbf{k}_2$ and $\mathbf{R}(j)$ can be expressed by $\mathbf{e}_C$ and $\mathbf{e}_T$ as follows:

$$\mathbf{k}_1=\mu_1|\mathbf{K}_1|\mathbf{e}_C+k_1\mathbf{e}_T,\quad \mathbf{k}_2=\mu_2|\mathbf{K}_1|\mathbf{e}_C+k_2\mathbf{e}_T,\quad \mathbf{R}(j)=\frac{\theta_j}{|\mathbf{K}_1|}\mathbf{e}_C+R_z(j)\mathbf{e}_T.\tag{A18}$$

Using Eq. (A18), we simplify the phase in Eq. (A16):

$$(\mathbf{k}_1-\mathbf{k}_2)\cdot\mathbf{R}(j)\pm\theta_j=(k_1-k_2)R_z(j)+(\mu_1-\mu_2\pm1)\theta_j.\tag{A19}$$

Taking the summation on j in Eq. (A16) we get $\delta(k_2-k_1)$ and $\delta(\mu_2-\mu_1\pm1)$. Finally, the optical matrix elment takes the following form:

$$\begin{aligned}\langle s_1,\mu_1,k_1|\mathbf{A}_q\cdot\nabla|s_2,\mu_2,k_2\rangle &= A_0\sum_{\ell,\ell'=A,B} C^{s_2*}_{k_2\mu_2\ell'}C^{s_1}_{k_1\mu_1\ell}\delta(k_1-k_2)\frac{1}{2}[\delta(\mu_1-\mu_2-1)+\delta(\mu_1-\mu_2+1)]\\ &\quad\times\sum_j\mathbf{n}_\perp\cdot\langle j,\ell'|\nabla|0,\ell\rangle e^{-i\mathbf{k}_2\cdot\mathbf{R}(j)}.\end{aligned}\tag{A20}$$

2. Parallel polarization

Similarly for parallel polarization, when we put Eq. (A13) in Eq. (A15), we get

$$\begin{aligned}A_0\mathbf{n}_{||}\langle s_2,\mu_2,k_2|\nabla|s_1,\mu_1,k_1\rangle &= \frac{A_0}{N}\sum_{\ell,\ell'=A,B} C^{s_2*}_{k_2\mu_2\ell'}C^{s_1}_{k_1\mu_1\ell}\sum_{\mathbf{j},\mathbf{j}'}e^{-i\mathbf{k}_2\cdot\mathbf{R}(j')}e^{i\mathbf{k}_1\cdot\mathbf{R}(j)}\mathbf{n}_{||}\cdot\langle j',\ell'|\nabla|j,\ell\rangle\\ &= \frac{A_0}{N}\sum_{\ell,\ell'=A,B} C^{s_2*}_{k_2\mu_2\ell'}C^{s_1}_{k_1\mu_1\ell}\sum_{j}e^{i((\mathbf{k}_1-\mathbf{k}_2)\cdot\mathbf{R}(j))}\sum_{j'}\mathbf{n}_{||}\cdot\langle j',\ell'|\nabla|j,\ell\rangle e^{-i\mathbf{k}_2\cdot(\mathbf{R}(\mathbf{j}')-\mathbf{R}(j))}.\end{aligned}\tag{A21}$$

Using Eqs. (A17)–(A19) we finally get

$$A_0\mathbf{n}_{||}\langle s_2,\mu_2,k_2|\nabla|s_1,\mu_1,k_1\rangle = A_0\sum_{\ell,\ell'=A,B} C^{s_2*}_{k_2\mu_2\ell'}C^{s_1}_{k_1\mu_1\ell}\delta(k_1-k_2)\delta(\mu_1-\mu_2)\sum_j\mathbf{n}_{||}\cdot\langle j,\ell'|\nabla|0,\ell\rangle e^{-i\mathbf{k}_2\cdot\mathbf{R}(j)}.\tag{A22}$$

APPENDIX B: DIFFERENT PLASMON BRANCHES

In Sec. III, we discuss plasmon spectra only for major plasmons, which appear first and remain dominant in terms of its magnitude. However, for $E_F > 2.0$ eV there exists another plasmon at the lower frequency as shown in Fig. 4(a). Now, in Fig. 10(a), we plot the absorption spectra $A_{\rm tot}=\mathrm{Re}(\sigma_\perp/\varepsilon_\perp)$, as well as EELS spectra by $\mathrm{Im}(-1/\varepsilon_\perp)$ (dash-dotted line), as a function of photon energy for the (10,5) SWNT at $E_F = 2.5$ eV. We can see two prominent peaks at 1.86 eV (peak 1) and 1.4 eV (peak 2), which differ by the dominant contributions [Fig. 4(a)], i.e., P_{35} (from A_{35}) and P_{24} (from A_{24}), respectively. In particular, for the peak 2, the absorption A_{35}, which is dominant for the peak 1, gives the negative contribution. This leads to a different behavior of the peak 2 as a function of E_F.

In Fig. 10(b), we plot $\varepsilon_1=\mathrm{Re}(\varepsilon)$, $\varepsilon_2=\mathrm{Im}(\varepsilon)$, $\sigma_1=\mathrm{Re}(\sigma)$, and $\sigma_2=\mathrm{Im}(\sigma)$ as a function of photon energy. The condition on plasmon excitation is satisfied at two zero points of the real part of dielectric function (solid vertical line). The absorption maxima (dotted vertical line) are red-shifted regarding to $\mathrm{Re}(\varepsilon)=0$, the shift is larger for peak 2, since ε_2 is steeper around ω_{p2}. Here we can clearly observe the effect of ε_2 on plasmonic spectra: $A_1/A_2\propto\varepsilon_2(\omega_{p2})/\varepsilon_2(\omega_{p1})$, where we denote A_1 and A_2 as the intensities of plasmon peaks 1 and 2. The presence of the second branch of intersubband plasmon have not been mentioned any of previous works of SWNTs. However, in recent years, several *ab initio*

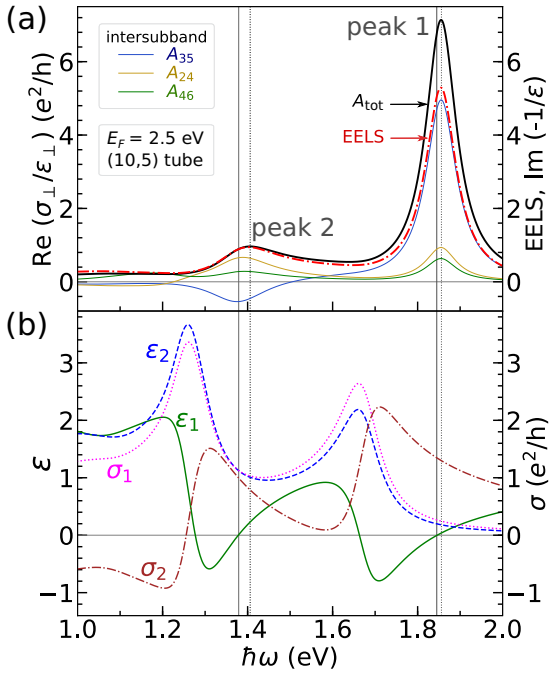

FIG. 10. (a) Absorption spectra for (10,5) doped SWNT with $E_F = 2.5$ eV. Black bold solid line represents the total absorption $A_{\rm tot}$. Colored solid lines correspond to the dominant A_{35}, A_{24}, and A_{46} intersubband contributions. The EELS spectrum, Im$(-1/\varepsilon)$, is plotted with red dash-dotted line. (b) Real and imaginary parts of dielectric function and conductivity for (10,5) doped SWNT with $E_F = 1.5$ eV. Solid vertical line corresponds to Re$(\varepsilon) = 0$, while dotted vertical line corresponds to max($A_{\rm tot}$).

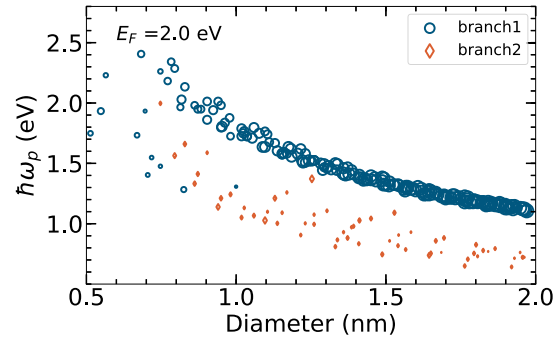

FIG. 11. Two plasmon branches in doped SWNTs. Blue circles correspond to the main branch discussed in Sec. III, orange diamonds correspond to the second branch plasmon, which appear at higher doping levels. The size of the marker corresponds to the peak intensity.

studies show the similar second branch for bilayer graphene, nanoribbons, and other 2D materials [55–58]. The intraband nature of the second branch plasmon in graphene nanoribbons was supposed by Gomez *et al.* [56], which is consistent with our results. We plot both plasmon branches for SWNT in Fig. 11 for different chiralities of SWNT with $d_t < 2$ nm at $E_F = 2.0$ eV. The lower plasmon peak P_{24} shows a larger chiral angle dependence since it comes from the cutting lines pairs closer to the K point than the major plasmon P_{35}. Thus the similar spreading character is observed for small-diameter SWNTs ($d_t < 1$ nm) and the second branch plasmon for bigger SWNTs ($1 < d_t < 2$ nm).

[1] H. Kataura, Y. Kumazawa, Y. Maniwa, I. Umezu, S. Suzuki, Y. Ohtsuka, and Y. Achiba, Optical properties of single-wall carbon nanotubes, Synth. Met. **103**, 2555 (1999).

[2] R. Saito, G. Dresselhaus, and M. S. Dresselhaus, Trigonal warping effect of carbon nanotubes, Phys. Rev. B **61**, 2981 (2000).

[3] S. M. Bachilo, M. S. Strano, C. Kittrell, R. H. Hauge, R. E. Smalley, and R. B. Weisman, Structure-assigned optical spectra of single-walled carbon nanotubes, Science **298**, 2361 (2002).

[4] R. B. Weisman and S. M. Bachilo, Dependence of optical transition energies on structure for single-walled carbon nanotubes in aqueous suspension: An empirical Kataura plot, Nano Lett. **3**, 1235 (2003).

[5] Ph. Avouris, J. Chen, M. Freitag, V. Perebeinos, and J. C. Tsang, Carbon nanotube optoelectronics, Phys. Status Solidi B **243**, 3197 (2006).

[6] Ph. Avouris, M. Freitag, and V. Perebeinos, Carbon-nanotube photonics and optoelectronics, Nat. Photonics **2**, 341 (2008).

[7] A. Kaskela, A. G. Nasibulin, M. Y. Timmermans, B. Aitchison, A. Papadimitratos, Y. Tian, Z. Zhu, H. Jiang, D. P. Brown, A. Zakhidov, and E. I. Kauppinen, Aerosol-synthesized SWCNT networks with tunable conductivity and transparency by a dry transfer technique, Nano Lett. **10**, 4349 (2010).

[8] A. P. Tsapenko, A. E. Goldt, E. Shulga, Z. I. Popov, K. I. Maslakov, A. S. Anisimov, P. B. Sorokin, and A. G. Nasibulin, Highly conductive and transparent films of $HAuCl_4$-doped single-walled carbon nanotubes for flexible applications, Carbon **130**, 448 (2018).

[9] H. Ajiki and T. Ando, Aharonov-Bohm effect in carbon nanotubes, Phys. B **201**, 349 (1994).

[10] J. Hwang, H. H. Gommans, A. Ugawa, H. Tashiro, R. Haggenmueller, K. I. Winey, J. E. Fischer, D. B. Tanner, and A. G. Rinzler, Polarized spectroscopy of aligned single-wall carbon nanotubes, Phys. Rev. B **62**, R13310(R) (2000).

[11] J. Jiang, R. Saito, A. Grüneis, G. Dresselhaus, and M.S. Dresselhaus, Optical absorption matrix elements in single-wall carbon nanotubes, Carbon **42**, 3169 (2004).

[12] Y. Murakami, E. Einarsson, T. Edamura, and S. Maruyama, Polarization Dependence of the Optical Absorption of Single-Walled Carbon Nanotubes, Phys. Rev. Lett. **94**, 087402 (2005).

[13] Z. M. Li, Z. K. Tang, H. J. Liu, N. Wang, C. T. Chan, R. Saito, S. Okada, G. D. Li, J. S. Chen, N. Nagasawa, and S. Tsuda, Polarized Absorption Spectra of Single-Walled 4 Å Carbon Nanotubes Aligned in Channels of an $AlPO_4$−5 Single Crystal, Phys. Rev. Lett. **87**, 127401 (2001).

[14] S. Uryu and T. Ando, Exciton absorption of perpendicularly polarized light in carbon nanotubes, Phys. Rev. B **74**, 155411 (2006).

[15] C. D. Spataru, S. Ismail-Beigi, L. X. Benedict, and S. G. Louie, Excitonic Effects and Optical Spectra of Single-Walled Carbon Nanotubes, Phys. Rev. Lett. **92**, 077402 (2004).

[16] F. Wang, The optical resonances in carbon nanotubes arise from excitons, Science **308**, 838 (2005).
[17] G. Dukovic, F. Wang, D. Song, M. Y. Sfeir, T. F. Heinz, and L. E. Brus, Structural dependence of excitonic optical transitions and band-gap energies in carbon nanotubes, Nano Lett. **5**, 2314 (2005).
[18] J. Jiang, R. Saito, K. Sato, J. S. Park, Ge. G. Samsonidze, A. Jorio, G. Dresselhaus, and M. S. Dresselhaus, Exciton-photon, exciton-phonon matrix elements, and resonant Raman intensity of single-wall carbon nanotubes, Phys. Rev. B **75**, 035405 (2007).
[19] K. Sasaki, S. Murakami, and H. Yamamoto, Theory of intraband plasmons in doped carbon nanotubes: Rolled surface-plasmons of graphene, Appl. Phys. Lett. **108**, 163109 (2016).
[20] K. I. Sasaki and Y. Tokura, Theory of a Carbon-Nanotube Polarization Switch, Phys. Rev. Appl. **9**, 034018 (2018).
[21] K. Yanagi, R. Okada, Y. Ichinose, Y. Yomogida, F. Katsutani, W. Gao, and J. Kono, Intersubband plasmons in the quantum limit in gated and aligned carbon nanotubes, Nat. Commun. **9**, 1121 (2018).
[22] R. Senga, T. Pichler, and K. Suenaga, Electron spectroscopy of single quantum objects to directly correlate the local structure to their electronic transport and optical properties, Nano Lett. **16**, 3661 (2016).
[23] R. Senga, T. Pichler, Y. Yomogida, T. Tanaka, H. Kataura, and K. Suenaga, Direct proof of a defect-modulated gap transition in semiconducting nanotubes, Nano Lett. **18**, 3920 (2018).
[24] R. Kuzuo, M. Terauchi, and M. Tanaka, Electron energy-loss spectra of carbon nanotubes, Jpn. J. Appl. Phys. **31**, L1484 (1992).
[25] R. Kuzuo, M. Terauchi, M. Tanaka, and Y. Saito, Electron energy-loss spectra of single-shell carbon nanotubes, Jpn. J. Appl. Phys. **33**, L1316 (1994).
[26] L. Papagno and L. S. Caputi, Electronic structure of graphite: Single particle and collective excitations studied by EELS, SEE and K edge loss techniques, Surf. Sci. **125**, 530 (1983).
[27] S. C. Liou, R. Breitwieser, C. H. Chen, W. W. Pai, G. Y. Guo, and M. W. Chu, π-plasmon dispersion in free-standing monolayer graphene investigated by momentum-resolved electron energy-loss spectroscopy, Microsc. Microanal. **20**, 1788 (2014).
[28] J. Hu, H. Zeng, C. Wang, Z. Li, C. Kan, and Y. Liu, Interband π plasmon of graphene: Strong small-size and field-enhancement effects, Phys. Chem. Chem. Phys. **16**, 23483 (2014).
[29] M. F. Lin and Kenneth W.-K. Shung, Plasmons and optical properties of carbon nanotubes, Phys. Rev. B **50**, 17744(R) (1994).
[30] M. F. Lin, D. S. Chuu, C. S. Huang, Y. K. Lin, and K. W.-K. Shung, Collective excitations in a single-layer carbon nanotube, Phys. Rev. B **53**, 15493 (1996).
[31] F. J. García de Abajo, Graphene plasmonics: Challenges and opportunities, ACS Photonics **1**, 135 (2014).
[32] I. V. Bondarev, Single-wall carbon nanotubes as coherent plasmon generators, Phys. Rev. B **85**, 035448 (2012).
[33] R. Saito, G. Dresselhaus, and M. S. Dresselhaus, *Physical Properties of Carbon Nanotubes* (Imperial College Press, London, 1998).
[34] M. Helm, The basic physics of intersubband transitions, in *Intersubband Transitions in Quantum Wells: Physics and Device Applications I*, Semiconductors and Semimetals, edited by H. C. Liu and F. Cappaso, Vol. 62 (Academic Press, San Diego, 1999) pp. 1–99.
[35] H. Ajiki and T. Ando, Electronic states of carbon nanotubes, J. Phys. Soc. Jpn. **62**, 1255 (1993).
[36] T. Nakanishi and T. Ando, Optical response of finite-length carbon nanotubes, J. Phys. Soc. Jpn. **78**, 114708 (2009).
[37] R. H. Ritchie, Plasma losses by fast electrons in thin films, Phys. Rev. **106**, 874 (1957).
[38] H. Raether, *Excitation of Plasmons and Interband Transitions by Electrons* (Springer-Verlag, Berlin, 1980).
[39] T. Igarashi, H. Kawai, K. Yanagi, N. T. Cuong, S. Okada, and T. Pichler, Tuning Localized Transverse Surface Plasmon Resonance in Electricity-Selected Single-Wall Carbon Nanotubes by Electrochemical Doping, Phys. Rev. Lett. **114**, 176807 (2015).
[40] H. Ehrenreich and M. H. Cohen, Self-consistent field approach to the many-electron problem, Phys. Rev. **115**, 786 (1959).
[41] R. Saito, A. Grüneis, Ge. G. Samsonidze, G. Dresselhaus, M. S. Dresselhaus, A. Jorio, L. G. Cançado, M. A. Pimenta, and A. G. Souza Filho, Optical absorption of graphite and single-wall carbon nanotubes, Appl. Phys. Lett. **78**, 1099 (2004).
[42] T. Hertel and G. Moos, Influence of excited electron lifetimes on the electronic structure of carbon nanotubes, Chem. Phys. Lett. **320**, 359 (2000).
[43] S. Reich, J. Maultzsch, C. Thomsen, and P. Ordejón, Tight-binding description of graphene, Phys. Rev. B **66**, 035412 (2002).
[44] R. Chegel, Third-nearest-neighbors tight-binding description of optical response of carbon nanotubes: Effects of chirality and diameter, J. Electron. Mater. **44**, 3500 (2015).
[45] V. N. Popov, Curvature effects on the structural, electronic and optical properties of isolated single-walled carbon nanotubes within a symmetry-adapted non-orthogonal tight-binding model, New J. Phys. **6**, 17 (2004).
[46] Ge. G. Samsonidze, R. Saito, A Jorio, M. A. Pimenta, A. G. Souza Filho, A. Grüneis, G. Dresselhaus, and M. S. Dresselhaus, The concept of cutting lines in carbon nanotube science, J. Nanosci. Nanotechnol. **3**, 431 (2003).
[47] R. Saito, K. Sato, Y. Oyama, J. Jiang, Ge. G. Samsonidze, G. Dresselhaus, and M. S. Dresselhaus, Cutting lines near the fermi energy of single-wall carbon nanotubes, Phys. Rev. B **72**, 153413 (2005).
[48] The plasmon data sets are open at http://github.com/DariaSatco/PlasmonOutput, while the absorption code is available at https://github.com/DariaSatco/cntabsorpt.
[49] K. Sato, R. Saito, J. Jiang, G. Dresselhaus, and M. S. Dresselhaus, Discontinuity in the family pattern of single-wall carbon nanotubes, Phys. Rev. B **76**, 195446 (2007).
[50] A. R. T. Nugraha, R. Saito, K. Sato, P. T. Araujo, A. Jorio, and M. S. Dresselhaus, Dielectric constant model for environmental effects on the exciton energies of single wall carbon nanotubes, Appl. Phys. Lett. **97**, 091905 (2010).
[51] K. Sato, R. Saito, A. R. T. Nugraha, and S. Maruyama, Excitonic effects on radial breathing mode intensity of single wall carbon nanotubes, Chem. Phys. Lett. **497**, 94 (2010).
[52] Ge. G. Samsonidze, R. Saito, N. Kobayashi, A. Grüneis, J. Jiang, A. Jorio, S. G. Chou, G. Dresselhaus, and M. S. Dresselhaus, Family behavior of the optical transition energies in single-wall carbon nanotubes of smaller diameters, Appl. Phys. Lett. **85**, 5703 (2004).

[53] E. H. Hwang and S. Das Sarma, Dielectric function, screening, and plasmons in two-dimensional graphene, Phys. Rev. B **75**, 205418 (2007).

[54] N. Sato, Y. Tatsumi, and R. Saito, Circular dichroism of single-wall carbon nanotubes, Phys. Rev. B **95**, 155436 (2017).

[55] M. Pisarra, A. Sindona, M. Gravina, V. M. Silkin, and J. M. Pitarke, Dielectric screening and plasmon resonances in bilayer graphene, Phys. Rev. B **93**, 035440 (2016).

[56] C. Vacacela Gomez, M. Pisarra, M. Gravina, J. M. Pitarke, and A. Sindona, Plasmon Modes of Graphene Nanoribbons with Periodic Planar Arrangements, Phys. Rev. Lett. **117**, 116801 (2016).

[57] Z. Torbatian and R. Asgari, Plasmon modes of bilayer molybdenum disulfide: A density functional study, J. Phys. Condens. Matter **29**, 465701 (2017).

[58] Z. Torbatian and R. Asgari, Plasmonic physics of 2D crystalline materials, Appl. Sci. **8**, 238 (2018).